INFRARED IMAGING

In 1800 Sir William Herschel, Royal Astronomer to King George III of England, wrote, "...There are rays coming from the sun ...invested with a high power for heating bodies, but with none for illumination objects ...The maximum of the heating power is vested among the invisible rays" (1). During his search for a new lens filter material to be used in telescopes for observing solar phenomena, Herschel recorded that some samples of colored glass that gave like reductions in brightness transmitted little of the sun's heat, whereas other samples transmitted so much heat that he felt impending eye damage after only a few seconds of observation. Herschel performed experiments with prisms and sensitive thermometers to determine which colors of the visible spectrum had the largest heating effect. Herschel recorded that the heating effect increased as the thermometer was moved from the violet to the red end of the spectrum.He continued to move the thermometer beyond the visible red end of the spectrum and saw an even greater temperature increase. The *dark heat* discovered by Herschel is known today as the infrared part of the electromagnetic (*EM*) spectrum (7). The prefix *infra* in this case refers to longer wavelengths, *below* or *beneath* (2) the red part of the visible region of the EM spectrum. The wavelengths of the EM waves in an infrared image typically range from 1 to 14 μm. Infrared radiation occupies the region of the electromagnetic spectrum between visible EM waves and radio waves. The range from three to five microns is called the *short-wavelength* band and the region from 8 to 12 μm is called the *long-wavelength* band.

The technology and science of infrared imaging have developed from Herschel's discovery in 1800 into a worldwide endeavor involving scientists and engineers from fields such as medicine, astronomy, material science, and the military. The technology of infrared imaging took a leap forward in 1917 when Case invented a *photoconductive* detector material capable of more efficiently detecting infrared radiation. Further improvements were made to the technology during World War II when it was discovered that the spectral sensitivity of the detectors could be broadened by cooling the photoconductive detector material below room temperature (1). Currently, the majority of fielded military IR imaging systems use similarly cooled detectors. Within the past ten years, however, a new imaging technology based on the pyroelectric effect has led to the development of uncooled IR imaging systems.

The usefulness of infrared imaging devices is based on a fundamental physical principle: heated objects emit infrared energy because of molecular agitation. The infrared energy emitted by the material object is called thermal radiance or radiation. The radiance or electromagnetic energy from the object itself is typically called the *signature* of that particular object. Each object has a unique signature. In a later section, the quantities used to characterize IR signatures are discussed. Several factors determine the magnitude of the thermal radiance emitted by an object. Some of these factors are the object's temperature relative to its environment, its surface reflectivity and its geometrical properties. In nature infrared energy is exchanged between objects when they absorb and radiate solar and heat energy from the atmosphere. Thermal energy from vehicles is released from the combustion of fuel inside engines and friction generated by moving parts. Heat from combustion and frictional heat cause ground vehicles to emit IR energy and hence have a *signature* in the IR spectrum unique to the vehicle's geometry and material characteristics. From a military point of view, a large IR signature aids in detecting a vehicle and is therefore usually to be avoided. Commercially, large IR signatures indicate energy loss, such as heat escaping through a region of poorly insulated ceiling or, in the case of electrical transmission wire, a region of wire nonuniformity that leads to increased ohmic resistance.

There are many applications of infrared imaging, such as medical research, astronomy, and remote sensing. Details of these areas can be found in books on these particular topics. The general principles involved in forming an IR image are discussed below.

THEORY OF INFRARED IMAGING

The EM spectrum encompasses wavelengths that span the range from very high-frequency gamma rays to low-frequency radio waves. Infrared radiation has wavelengths just beyond the red part of the spectrum. Most of the observed phenomena in the visible region are related to the reflected sunlight or artificial illumination. Most infrared phenomena are related to radiation emitted from objects. The radiation emitted is related to temperature. The well-known relationship between temperature and radiation, known as the Stefan–Boltzmann law of radiation, is obtained by integrating Planck's formula from $\lambda = 0$ to $\lambda = \infty$. The total radiant exitance by a blackbody is given by

$$W_b = \sigma T^4 (\mathrm{W/m^2}) \tag{1}$$

where σ is the Stefan–Boltzmann constant, 5.67×10^{-8} $W/(\mathrm{m}^2K^4)$. Every object in the universe is constantly emitting and receiving IR radiation as thermal radiation from every other object. The amount of radiated energy varies depending on the temperature and emittance of its surfaces. The laws governing the radiation, transmission, and absorption of infrared radiation are part of thermodynamics and optics. This infrared radiation can be used for imaging devices that convert an invisible infrared image into a visible image. Human vision can be extended beyond the visible red part of the EM spectrum with a thermal imaging system.

Historically, after the emergence of television after World War II, camera tube principles were applied to night-vision systems. The source radiation for IR imaging may be self-emitted from objects in the scene of interest or reflected from other sources. Sunlight is the primary source of reflected radiation. Another may be from controlled sources, such as lasers, used specifically as illuminators for the imaging device. Those systems with sources that illuminate part of the scene are called active, whereas those relying largely on radiation emitted from the scene are called passive. A passive IR imager is an electrooptical system that accomplishes the function of remote imaging of the scene without active scene illumination. Figure 1 is a block

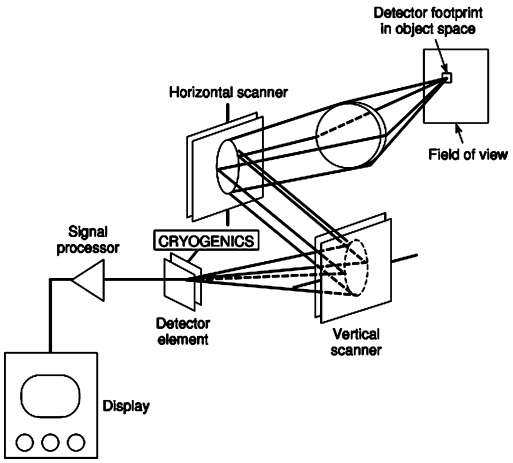

Figure 1. Block diagram of a passive IR sensor.

diagram of a passive infrared imaging system. To describe the electronic operation of IR sensors, it is often easier to use the particle nature of light, that is, photons. A photon's path is through the sensor from the scene element source, then on through the optics and detector which ends with its conversion to an electronic signal at the focal-plane array (*FPA*). The photon-generated signals are processed to obtain useful information which is displayed as an image by infrared image processing.

It will be helpful to the reader to begin a detailed discussion of a passive imaging system by clarifying signal processing versus image processing. The division between signal processing and image processing is blurred by the applied architecture and end application. Signal processing usually refers to the time stream of data coming from a single detector, much like the line trace of a heartbeat on an oscilloscope. Signal processing works on and looks at the rise and fall of the trace to detect targets against the background noise (5). Diagrams of IR signal processors are given in Ref. 3. Infrared imaging has found application in such diverse fields as medicine, nondestructive material evaluation, astronomy, and robotics. As such, a large degree of image processing is needed. The following describes some of these steps for infrared image processing.

INFRARED IMAGE PROCESSING

Now we consider what happens after the sensor has converted photons to representative signals. The output of the focal plane's multiplexer is analog electrical signals. The signals may be amplified and converted into digital signals and conditioned and processed to form images or targeting information. The following are the special considerations needed to create a clear image as given in (5):

1. Correction To smooth out the response of the individual pixels that make up the FPA and make the response more uniform is one of the most important signal processing functions. Most FPA's require a two-point correction that adjusts each pixel for both gain and offset by recording the response of the FPA as it *stares* at two known radiance sources of blackbodies at two different temperatures.
2. Calibration When some radiometric applications use three- and four-point correction, calibration is needed. Calibration adjusts system parameters to known standards which are the standard blackbody sources.
3. Ac Coupling Ac coupling removes a pedestal of noise. This allows identifying a smaller temporal spike more easily on top of a large, constant signal platform. This removes the constant amplitude component of the scene and, in the temporal domain, passes only changes.
4. Dc Coupling Dc coupling works similarly for constant radiation and staring sensors. A dc-coupled signal with a low-pass filter reduces large fluctuations and passes the constant background. This approach is often used with staring sensors.
5. Thresholding This technique compares a pixel value with some threshold value. If the value is higher than the threshold value, it will be identified as a possible target pixel. Thresholding for focal-plane frames falls into the category of image processing.

Image processing deals with the differences between adjacent scene pixels in a two-dimensional arrangement of detectors, and it generally includes the time-changing components of signals. Usually, a level of signal processing (such as nonuniformity correction) occurs before other higher order image processing functions, such as edge detection. A primary factor to remember is that signal processing is single-detector element or pixel-related, whereas image processing relates to multiple pixel configurations. Image processing also refers to operations that transform images into other images. Image recognition is the mapping of images into descriptions. Image transformations convert matrix A into another matrix B called the transform image. The image B is computed to extract features, which are characteristic elements (geometrical, IR light intensities) in the image, to classify objects or targets in the scene. The following are some basic image processing techniques and functions and their corresponding techniques (5):

1. Spatial Filtering Spatial filtering removes false targets (reduction of clutter) using a weighted average of the signal from neighboring pixels to determine a localized mean. This localized mean sets an adaptive threshold to determine whether the pixel belongs to a targetlike object. Temporal filtering performs the same in the time domain for each pixel. This process is equivalent to a type of spatial filter for a scanning system and a frame-to-frame subtraction for a staring sensor. Morphological filtering is a spatial filtering technique which uses a specific one-dimensional or two-dimensional operator to detect objects of a given spatial frequency.
2. Frame-to-Frame Subtraction In frame-to-frame subtraction, one frame is simply subtracted from another taken at a different time.

3. Streak Detection Streak detection is a higher order form of frame subtraction indicating moving targets. In streak detection, a pixel and its neighbors are compared from frame-to-frame in the time domain.
4. Image Formation Image formation consists of taking the FPA output and forms an image.

IR target features used for classification are characterized by the fact that some are geometric and others statistical in nature. The recognition process involves a tree-type decision process adapted to each set of target classes. Using those features by which each class is best discriminated from others, such a procedure first starts with well-discriminated classes and ends with overlapping classes. Such a hierarchical classification procedure, represented by a tree structure, consists of specified feature extraction and decision rules. The individual decisions in a classification tree may rely on one or more of the following approaches (4):

1. Template matching of features derived, respectively, from feature extraction and learning
2. Statistical pattern recognition
3. Syntactic pattern recognition
4. Hybrid pattern recognition and artificial intelligence for scene understanding.

INFRARED SYSTEMS AND ARRAY GEOMETRIES

In order to form IR images, several array geometries are possible. There are several established methods for designing practical IR images. Table 1(10) summarizes the various architectures used in infrared systems and the distinguishing features of each generation of system.

Focal-Plane Arrays

The focal plane is perpendicular to the optic axis where the IR radiation is focused in an imaging system. An array of detectors located there is a focal-plane array (*FPA*). The focal-plane array consists of densely packed detector elements numbering up to 10^6 or more. A FPA may contain several FPA sections connected together. Occasionally, a focal plane is curved about the Petzval surface (57) using more than one focal-plane array. A group of focal-plane arrays is called a mosaic. The evolution of infrared detectors suitable for forward-looking infrared (*FLIR*) systems is shown diagrammatically in (11). FLIRs are IR images that form an image of the scene directly in front of the camera. Large arrays are usually made from photovoltaic detectors. The photovoltaic detector lends itself more to large arrays because of its lower thermal power dissipation. Photovoltaic operation also provides a square root of two improvement in noise over a photoconductive detector, simpler biasing, and more accurately predictable responsivity. Most focal-plane assemblies are constructed by using detector chips with, for example, 640×480 detector elements. These can be monolithic (detector and signal processor in a single semiconductor crystal) or hybrid (detector and signal processor in separate materials interconnected by solder bump bonds and/or evaporated fan-out patterns) (5).

Uncooled Systems

Uncooled infrared focal planes are fundamentally different from cryogenically cooled systems (55). Uncooled focal planes are two-dimensional arrays of infrared detectors thermally isolated from their surroundings. The detectors respond to incoming infrared radiation by changing their temperature. The materials used for these detectors are chosen for certain unique properties, such as resistance, pyroelectric polarization, or dielectric constant that varies sharply with temperature.

A pyroelectric material has an inherent electrical polarization. The magnitude of the polarization is a function of temperature (56). In a pyroelectric material polarization vanishes at the Curie temperature. The pyroelectric coefficient p is defined as the gradient of electrical polarization as a function of temperature. A simple pyroelectric detector consists of a wafer of this material with metal electrodes bonded on each face. The material is oriented so that the polar axis is perpendicular to the electrodes. As the temperature of the pyroelectric material is changed by incident radiation, its polarization changes in direct proportion to the magnitude of the temperature change. Charges accumulate on the electrodes, and a voltage develops across the faces of the pyroelectric material, just as in a capacitor. The charge or voltage residing on the material is a function of the incident irradiation by IR energy. An imaging sensor is accomplished using this detector array by adding a "chopper" to introduce a known change in the incident radiation and hence voltage across the material.

Currently, two different types of detector, one ferroelectric and the other bolometric, are used for uncooled, focal-plane arrays. The approach followed by Raytheon is to use a ferroelectric material. An array of detectors is made with a ferroelectric material having polarization and dielectric constants that change with temperature, resulting in a change in charge on a capacitor as the target scene varies. The detectors are fabricated from the ceramic material, barium strontium titanate (*BST*), and then bump bonded to a silicon readout circuit. The approach uses a two-dimensional array of bolometers, resistors whose resistance changes approximately 2% per $^\circ$C change. The temperature-sensitive resistor material is vanadium oxide, suspended on a bridge of silicon nitride that is isolated thermally from the substrate containing the readout electronics.

These uncooled, focal-plane systems perform robustly enough to make them suitable for many military and commercial applications. An example of a road scene taken with a pyroelectric device is shown in Fig. 19. One development option is to reduce the detector size even further, thus producing better resolution with the same optics. Sensitivity improvements are also desirable and achievable. For applications where the sensitivity is already satisfactory, the increased sensitivity could be traded for slower (i.e., smaller, lighter, and less expensive) optics. Additional development is expected to result in decreased electrical noise and smarter focal planes (3, 5).

Table 1. Features of Various Infrared Imaging Systems

Generation	Distinguishing Characteristics	Remarks
First	Uses a scanned, linear detector array to generate real time imagery	Uses photoconductive detector elements; common modules use parallel linear arrays of 60, 120, or 180 detector elements; most often uses analog processing but can use digital
Enhanced First	Uses detector arrays with improved sensitivity compared to first-generation common modules	Usually the detectors are advanced photoconductive structures such as ``SPRITE'' detectors
Second	Uses two-dimensional arrays of detectors and on-chip multiplexing at the focal plane to read out the detector signals with reduced lead count for real time imaging	Usually has photovoltaic detector elements; includes both scanned and staring arrays; includes, but is not limited to, HgCdTe, InSb, PtSi, and uncooled IR detector materials
Third	Provides image processing at or near the focal plane and/or multiband real time imaging capability; multiband includes optical and millimeter wavelengths	Uses a ``smart'' focal plane array.

METRICS IN CLUTTERED IMAGE ENVIRONMENTS

Many perceptual measures used by the US Army (12, 13) and other armed forces exist for assessing the visibility of vehicles as seen by a human through an infrared sensor and electronic display. These measures have a limited range of applicability because the measures usually work only for a restricted class of images. The focus of this article is algorithms for optimal measures of thermal contrast, target temperature minus background temperature (ΔT), and clutter. The detection of vehicles by an IR sensor is essentially the problem of detecting such vehicles in a cluttered background. The purpose of defining and quantifying clutter is to aid the development of more realistic human detection models. In one way or another, most of the work on *clutter measures* or *metrics* has depended on or grown from a metric defined by Schmeider–Weathersby (*SW*) (14). The SW clutter metric is written as follows:

$$\text{Clutter} = \sqrt{\sum_{i=1}^{N} \left(\frac{\sigma_i^2}{N} \right)} \tag{2}$$

where σ_i is the variance of the ith cell and N is the number of cells. The SW clutter metric divides the image into a number of cells, each of which are scaled to represent twice the longest dimension of the target, and then the variance of each cell is divided by the total number of cells.

Clutter

The clutter and temperature difference between the target and background (ΔT) metrics are discussed first because together, clutter and ΔT metrics form the signal-to-noise ratio (SNR) used in evaluating the probability of detection (*Pd*). A large part of the framework for the present methodology for calculating *Pd* is based on signal detection theory (*SDT*). The use of SDT in an area of modeling requires a clear distinction between what is to be the *signal* and what is to be the *noise.* The delineation of the *target* in an image constitutes deciding what the signal is to be. Everything else is taken as the noise. As described further in this article, clutter is considered a noise term. Objects in the image which distract the observer from the target or get attention

because they are similar to the target are called clutter.

Clutter Metrics

Objects and background regions in an image that look similar to or that distract from the actual target(s) are known as *clutter*. To date there has been a lot of work to develop a quantitative measure of background clutter (15–30). Reynolds et al. (17) analyzed many scenes of northern rural Michigan and calculated the aforementioned SW clutter in those scenes as a function of field measured environmental variables, such as wind speed, humidity, insolation, and temperature. For groups like the US Army, who are concerned with how vehicles appear in open terrain, the difficulty of controlling the parameters measured in the field motivates the use of computer modeling. Hence a large part of clutter research is geared toward finding insights to understand the interaction of environmental variables and clutter with the aid of computer modeling so as to reduce the need for taking field data. The goal is to link clutter with human perception and the probability of detection. There are many definitions of clutter currently used in the literature of image processing and target acquisition modeling (18, 19). Some of these metrics follow:

(mean target) − (mean background) radiance or ΔT metric

1. Statistical variance metric (*SW* clutter)
2. Probability of edge (*POE*) metric
3. Complexity metrics

There is presently no definition available which is clearly the best in all cases or images. One primary object of this section is a unified definition of clutter which takes into account the different definitions available in the literature. Many of the images used for study in this article were obtained from the US Army's Night Vision Lab (*NVL*) terrain board simulator. The terrain board simulator is a large room painted entirely black which has a scaled-down version of the terrain of a certain part of the world at the center of the room. Genuine infrared and visual sensors are then placed at certain positions. On the terrain board are placed scaled-down vehicles painted with an emissive coating to emulate the actual appearance of the vehicles as seen through night vision cameras. Pictures are then taken with the mounted night-vision cameras and displayed on monitors in target perception experiments. As part of the review of the phenomenology associated with clutter metrics, a few of these metrics are described here. Currently used clutter and image metrics are the following: Der metric, POE metric, the Schmieder–Weathersby metric, and texture-based clutter metrics.

Der Clutter Metric. Originally the Der metric was devised as a method to predict the false alarm rate of a given algorithm. The approach was the following: a double window was convolved one pixel at a time over the image. The size of the inner window was the maximum size of the largest target used at the time. These two features, minimum and maximum, were chosen arbitrarily. At each pixel location, the algorithm decides whether the new pixel is in the same intensity space as the one previously examined and then also whether it fits into the inner window. When an intense region of the image of approximate target size is found, that region is catalogued. The principle behind the Der method then is to multiply the distribution of the target like areas by the probability-of-detection distribution. Then the result should give the predicted false alarm rate for an algorithm with a given probability-of-detection distribution. Now if one simply counts the number of Der objects in the image, that number should indicate the number of targetlike objects in the scene, and hence, a measure of clutter (18).

POE Metric. The probability of edge (*POE*) metric is meant to determine the relationship between the human visual detection system and the statistics of the color or black and white images. First, the image under consideration is processed with a difference-of-offset-Gaussian (*DOOG*) filter and is thresholded. This procedure emulates the early vision part of a human observer (20), basically just the retinal part of human color vision. Then the number of edge points are counted and are used as the raw metric. The calculation proceeds as follows. First, the image is divided into blocks twice the apparent size of the target in each dimension. Then, a DOOG filter, as described in (21), is applied to each block to emulate one of the channels in preattentive vision. The net effect is to enahance the edges. As discussed by Rotman et al. (22), the histogram of the processed image is normalized and then a threshold T is chosen on the basis of the histogram. The number of points exceeding the threshold in the ith block are computed as $\mathrm{POE}_{i,T}$. Then the POE metric is computed similarly to the statistical variance technique:

$$POE = \frac{1}{N}\sum_{i=1}^{N} POE_{i,T}^2 \tag{3}$$

Marr (20) and other vision researchers have recognized that preattentive vision is highly sensitive to edges.

Schmieder and Weathersby (*SW*) Metric. Schmieder and Weathersby (14) have proposed the concept of a root-mean-square (*rms*) clutter metric of the spatial-intensity properties of the background. It is one of the most commonly used clutter measures. The Schmieder and Weathersby clutter metric, shown in Eq. (2), is computed by averaging the variance of contiguous square cells over the whole scene.

Typically N is defined as twice the length of the largest target dimension. The signal-to-clutter ratio (*SCR*) of the image is then given by the average contrast of the target divided by the clutter computed in Eq. (2).

Reynolds (15) showed that the variance in Eq. (2) is equivalent to the following:

$$\frac{1}{Nk}\sum_{i=1}^{N}\sum_{j=1}^{k}(x_{ij}-\mu)^2=\frac{1}{N}\sum_{i=1}^{N}(\mu_i-\mu)^2+\frac{1}{Nk}\sum_{i=1}^{N}\sum_{j=1}^{k}(x_{ij}-\mu_i)^2 \tag{4}$$

where N is the number of cells, k is the number of pixels per cell, x_{ij} is the radiance of the jth pixel in the ith cell, and u_i is the ith cell mean radiance. Doll (23) compared Eq. (2) with experimental detection times for observers looking at computer-generated images of rural scenes with embedded targets. Good correlation between the average detection time and SCR value was found. One of the fundamental problems of computer-based vision is that the contrast metrics are valid only for a limited group of images.

Texture-Based Clutter. As mentioned previously, the purpose of defining and quantifying clutter is to aid the development of more realistic human-detection models. Clutter is sometimes defined in the sense that areas of similar texture contribute to the distractive capability or clutter of a scene. Textural measures of a scene are potentially very powerful metrics for extracting fine-level, contrast differences in an image and play a crucial role in modeling human visual detection. The scene used for this study of texture and clutter was from the standard scene collections of the Keewenaw Research Center of Michigan Technological University, KRC83-1-1.dat. The thermal image contains an M60 tank in a field with a tree background. The basic scene was altered with the Geographics Resources Analysis Support System (*GRASS*) software package so that there were three scenes with different amounts of clutter, low, medium, and high, respectively. Low, medium, and high clutter were defined as equal to one, three, or nine false targets in the field of view (*FOV*) containing the vehicle (23).

In Fig. 2, pictures A through C are the original input cluttered IR scenes, and pictures D through F are the computer-modeled IR sensor field of views of the low, medium, and high cluttered scenes, respectively. The three images mentioned were read into the TARDEC Thermal Image Model (*TTIM*) (24). TTIM is a graphics workstation model that uses measured or simulated target-in-scene IR imagery as input. TTIM has been used to simulate the image degradation introduced by atmospheric and sensor effects (25, 26) at a specified range. TTIM transforms the degraded radiance values on a pixel-by-pixel basis to gray-scale values for display on a workstation for observer interpretation and/or further processing.

Equation (2) was used to calculate the variance-based clutter in the images, also known as the Schmieder–Weathersby (*SW*) clutter. The cell size chosen was twice the maximum target dimension which was always the length in pixels of the vehicle. The clutter and textural data were then input into statistical and graphing tools for further analysis. The standard clutter SW definition of clutter was modified to include image texture by calculating the gray-scale texture for each cell and then using that texture in place of the variance. The method of calculating texture was based on the equation given in (27). To compute the SW variance-based clutter, the image is divided into cells twice the maximum target dimension. Then the variance is computed for each cell and aggregated, as described by (30). At a given resolution, a block of pixel values is recorded and the variance of the gray-scale values is formed. Then the rms is taken over the entire image. The equation modified for the digital computation of textural clutter is shown in Eq. (5):

$$T(j,k,r,\theta)=\sum_{a=0}^{L-1}\sum_{b=0}^{L-1}P(a,b:j,k,r,\theta) \tag{5}$$

where a and b are any two gray-scale values at any pixel (j, k) in the image matrix, r is the step size, and θ is the direction of the steps (θ equals 0 means stepping horizontally). P is the fraction of the total number of steps whose end points are the gray-scale values a and b, respectively. The mean texture is defined as follows:

$$M_T(j,k,r)=\frac{1}{N_\theta}\sum_\theta T(j,k,r,\theta) \tag{6}$$

Defined in the above manner, texture is considered the spread about the diagonal of the cooccurrence matrix (28). As the clutter in the image increases, the spread of the wings of the central region in the textural plot increases, indicating an increase in texture which would be expected if the clutter in the image increases. The modified clutter equation that includes mean texture follows:

$$\text{Clutter}=\sqrt{\sum_{i=1}^{N}\frac{\frac{1}{N_\theta}\sum_\theta T_i(j,k,r,\theta)}{N}} \tag{7}$$

The performance of the textural metric as a function of several variables has been described by (28). The first data set consisted of four variables: (1) wind speed, (2) turbulence, (3) humidity, and (4) temperature difference between the target and background. The second data set included spectral bandpass, turbulence, rain rate, and temperature difference between the target and the background. The experimental design was chosen to include all of the variables so that the least amount of simulations would be required. A fifth variable, texture, was computed for each point in the experimental design. Clutter was modeled as a second-order response surface in the original five variables. Stepwise regression was used to build the model and residual analysis was done to check the assumptions of the model.

Some general remarks concerning the nature of the images generated by the sensor and atmospheric models used are appropriate. For the second parameter set, gray-scale levels of the output images were manually scaled. In other words, for each clutter class, the minimum and maximum temperature values for the extreme parametric cases were recorded in advance to provide a temperature/gray-scale range for the entire image set. Otherwise, the autoscale function would be used and the image contrast would always be maximized for each image rather than having a gray scale appropriate to the entire range of pixel temperatures for the parameter variations. The clutter and textural calculations all used the gray-scale values written from the screen to the hard disk. For all clutter classes, low,

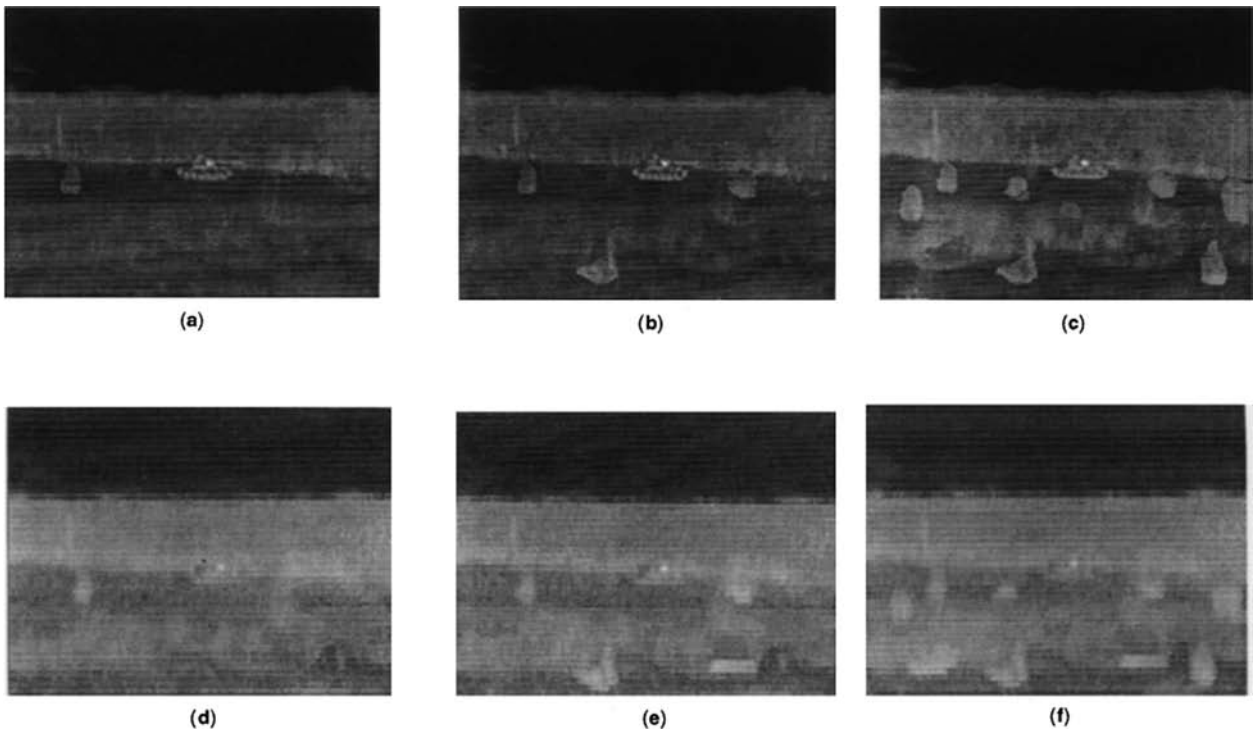

Figure 2. A, B, C: original images with low, medium, and high clutter and TTIM. D, E, and F: simulations.

medium, and high, the calculated clutter values decreased as the parameters increased. The modeled sensor scene became more homogenous or lower in contrast, and the target was more difficult to distinguish. Thus the probability of detection can decrease even while the clutter, defined as a variance of gray-scale values in a cell, is decreasing.

The results of the simulations showed that for the SW clutter metric, temperature difference, rain rate, and texture were the most important parameters. For the texture-based clutter metric, temperature difference, rain rate, and spectral bandpass were important. When the SW clutter was plotted versus the texture-based clutter metric, the result was a straight line. This result is unexpected because the two methods of calculating clutter are very different. The SW clutter metric is a variance of the pixel gray-scale values in the image and the texture-based clutter metric involves the cooccurrence matrices of the gray-scale values in the image. These two measures may give nearly similar results when the amount of texture in the scene is small. Perhaps by increasing a feature in the scene, such as the periodicity or scene complexity, the two texture measures would generate more different results. A representative graph of the two measures for the highly cluttered scene is shown in Fig. 3.

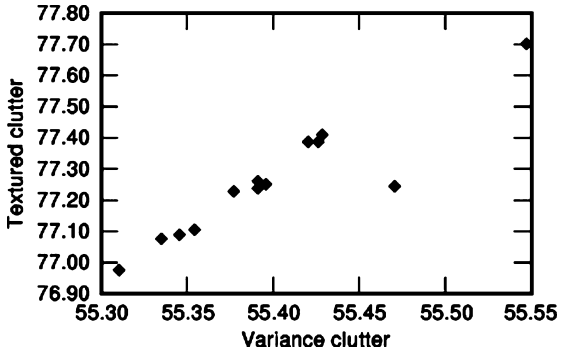

Figure 3. Plot of textured clutter versus SW clutter.

Relative Metrics in the Probability of Detection

Rotman et al. (29) reviews the NVL model for computing the probability of detection P_d and suggests a way to include clutter in the algorithm for P_d. However, no mention is made of how to compute the properly scaled clutter factors alluded to in the paper. A method for obtaining clutter factors based on other validated clutter measures that can be used in this equation is described next. As described by Rotman et al. (29) and Gerhart et al. (34), the probability of acquisition of a target as a function of time is given by the following:

$$P(t) = P_\infty \left[1 - \exp\left(\frac{-P_\infty t}{3.4}\right)\right] \tag{8}$$

or

$$P(t) = \frac{\rho}{\mathrm{CF}} \left[1 - \exp\left(\frac{-(\rho/\mathrm{CF})t}{3.4}\right)\right] \tag{9}$$

In Eq. (9), ρ is an estimate of the target acquisition probability over an infinite amount of time when the target is in the field of view, and

$$\rho = \frac{(n/n_{50})^E}{1 + (n/n_{50})^E} \tag{10}$$

where n is the number of resolvable cycles across the target, n_{50} is the number of cycles required for P_∞ to equal 0.5, E is equal to 2.7 + 0.7 (n/n_{50}), and CF is a clutter factor. Clutter is a term that refers to the psychophysical task of perceiving objects in a scene in the presence of similar objects (15). Clutter factor refers to the number used to represent how many target-like objects there are in the image which confuse the viewer as to the location of the target. Rotman (29) has shown that

$$\left(\frac{n}{n_{50}}\right) = \frac{\ln\left[\dfrac{\Delta T\sqrt{\epsilon/7}}{MRT_0} - R\beta_{atm}\right]}{\dfrac{\gamma}{s}\,\beta_{sys}R} \tag{11}$$

Hence, Eq. (9) can be written as a function of ΔT and the clutter factor CF. Or the probability of detection $P(t)$ can now be computed as a function of ΔT, the range from the target to the sensor, the atmospheric condition, and the sensor system parameters. Figure 4, courtesy of Dr. Barbara O'Kane of Night Vision Electrooptic Sensor Directorate (NVESD), is one of the images used in this study. The target is in the foreground.

EQUIPMENT AND EXPERIMENTAL METHODS

Throughout this section, reference has been made to experimental values of P_d. A discussion is now given of what this entails. The experimental determination of the P_d for a target in a cluttered image is determined by using displayed images on a rear-projection screen or computer monitor. Basically, the observer sits at a distance of 1 meter away from a large, high-resolution display monitor in a darkened room or area and glimpses the images for about 1 s. The subject is given training before the tests and is told what to expect in the way of imagery and targets. All of the visual detection tests test foveal detection, that is, detection of an object in a scene directly in the line of sight of the subject. Foveal detection is important for static scene detection, whereas peripheral viewing is often important for detecting motion. The observers are then asked whether they did or did not see a target of interest (military or otherwise), and/or if the observers are not sure and would like to see the image(s) again. This is called a forced-choice experimental design. The images in a particular data set are displayed at random, and the responses of the individual subjects are tallied electronically and used to calculate a probability of detection and of false alarm of the target of interest for the given experiment and for that particular subject. A typical collection of subjects is 10 to 15 and a typical number of images is 15 to 100. The separate subjects' responses, or P_d's, for each target are also used to calculate a population mean probability of detection and probability of false alarm for each target. Psychophysical detection experiments have been performed, using this pilot test lab, for part of the US Army's visual acquisition model validation and verification programs and for a Cooperative Research And Development Agreement (*CRADA*) between TARDEC and an automobile company on vehicle conspicuity. Throughout the tests mentioned, a small cubicle was used as the experimental area. A schematic of the test setup is shown in Fig. 5. Recently at TARDEC, a visual perception laboratory (*VPL*) large enough to enclose vehicles and three large rear projection screens has been built to perform visual and infrared detection tests. A later section describes and shows the TARDEC VPL.

WAVELET TRANSFORMS OF IR IMAGES

Introduction

There are many important characteristics of wavelets that make them more flexible than Fourier analysis. Fourier basis functions are localized in frequency but not in time. Small frequency changes in a FT cause changes everywhere in the time domain. Wavelets can be localized in both frequency position and in scale by dilation and in time by translations. This ability to perform localization is useful in many applications (31). Another advantage of wavelets is the high degree of coding efficiency or, in other words, data compression available. Many classes of functions and data can be represented very compactly by wavelets. Typically the wavelet transforms are computed at a faster rate than the fast Fourier transforms (*FFT*s). The data is basically encoded into the coefficients of the wavelets. The computational complexity of the FFT is of the order of $n \log n$, where n is the number of coefficients, whereas for most wavelets, the order of complexity is of the order n. Many data operations, such as multiresolution signal processing, can be done by processing the corresponding wavelet coefficients (31). The basic flow of processing in wavelet analysis is shown in Fig. 6.

Wavelet Transforms and Their Use with Clutter Metrics

Wavelets and wavelet transforms are essentially an elegant tool that can be applied to image processing. Wavelets are used for removing noise or unwanted artifacts from IR images as well as acoustic data (31, 32) or for localizing certain target cue features. There are many definitions of clutter currently used at the moment (30). However, none take into account the multiresolution capability of wavelets. A way to do this is by using edge points determined by wavelets (30, 33). The P_d can be computed using the signal-to-clutter ratio (SCR) as in the classical theory. Then the computed P_d values can be correlated to the experimentally determined P_d for the target. As discussed in (22, 34), the classical algorithm for the determination of the P_d of a target in an image is shown in Eqs. (8), (9), (10), and (11). The idea proposed by (30) is to use wavelets in the clutter factor so that the noise term is replaced by an interference term that includes noise plus clutter. The wavelet probability of the edge (*WPOE*) algorithm was applied to many IR images with a combination of a personally developed code and the software package XWAVE2 (35) installed on a Silicon Graphics Indigo2 workstation running IRIX 5.03. For input images, Night Vision Lab's (*NVL*) terrain board images, developed and shared by Dr. B. O'Kane, C. Walters, and B. Nystrom (12) were used. A sample of this data from the NVL set is shown in Fig. 4. The image was segmented by cell, and a wavelet transform was applied to

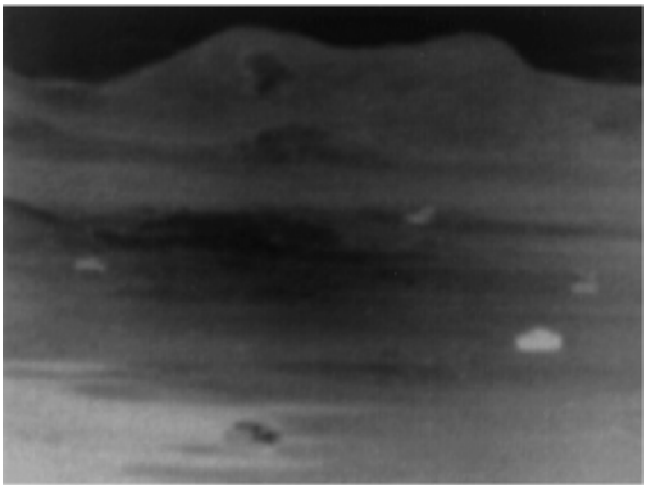

Figure 4. NVESD terrain board image (from Dr. O'Kane).

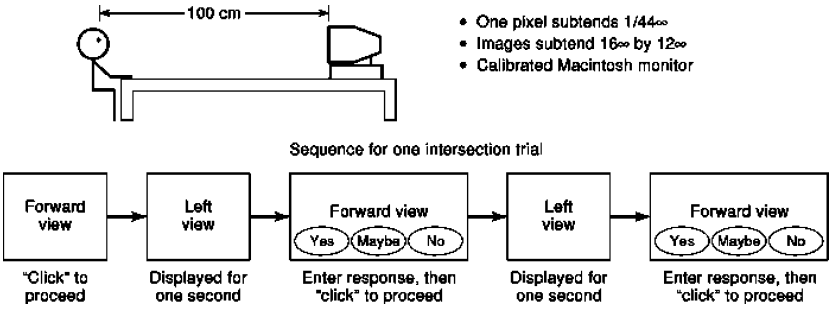

Figure 5. Pilot perception test setup.

Figure 6. Flow of processing in wavelet analysis of IR images.

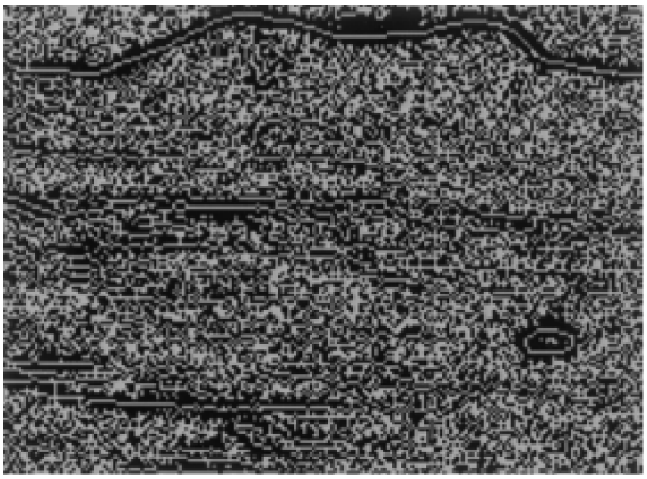

Figure 7. NVESD image level 1.

find the number of edge points at a particular scale. Figures 7,8, and 9 are the wavelet transforms of the entire IR image. After processing the image with the wavelet filters, what is required is the number of edge points above a certain threshold in each of the cells of the wavelet image and at a particular resolution level. A cell is composed of an array of pixels taken together generally forming a square or rectangular figure. With the number of edge points per cell and the total number of points or pixels in the cell, the WPOE can be computed. The WPOE clutter metric is used in the denominator of the SNR to compute the probability of detection of the target. For the IR case, the signal is the difference of the mean temperature of the target and background, and the noise term is a clutter metric, such as the POE, WPOE, or RMS clutter. A new metric, the WPOE metric, and an algorithm for computing clutter in infrared and visual images was used in (30). There are some problems that must be resolved, such as thresholding and further re-

Figure 8. NVESD image level 2.

Figure 9. NVESD image level 3.

duction of the cell size, but the method of the WPOE metric is of potential use in image analysis.

FUZZY LOGIC AND DETECTION METRICS FOR IR IMAGES

It has been three decades since L. A. Zadeh first proposed fuzzy set theory (logic) (36). Following Mamdani and Assilian's pioneering work in applying the fuzzy logic approach (*FLA*) to a steam engine in 1974 (37), the FLA has been finding a rapidly growing number of applications. These applications include transportation (subways, helicopters, traffic control, and air control for highway tunnels), automobiles (engines, brakes, transmission, and cruise control systems), washing machines, dryers, TVs, VCRs, video cameras, and other industries including steel, chemical, power generation, aerospace, medical diagnosis, and data analysis (38–42). Although fuzzy logic encodes expert knowledge directly and easily using rules with linguistic labels, it usually takes some time to design and tune the membership functions which quantitatively define these linguistic labels. Neural network learning techniques can automate this process and substantially reduce development time and cost while improving performance. To enable a system to deal with cognitive uncertainties in a manner more like humans, researchers have incorporated the concept of fuzzy logic into the neutral network modeling approach. A new approach to computing the probability of target detection in infrared and visual scenes containing clutter by fuzzy logic is described in Ref. 30.

At present, target acquisition models based on the theory of signal detection are not mature enough to robustly model the human detection of targets in cluttered scenes because our awareness of the visual world is a result of perceiving, not merely detecting, the spatiotemporal, spectrophotometric stimuli transmitted onto the photoreceptors of the retina (43). The computational processes involved with perceptual vision can be considered the process of linking generalized ideas or concepts to retinal, early visual data (43). These ideas or concepts may be various clutter or edge metrics and luminance attributes of a military vehicle or automobile. From a systemic theoretical viewpoint then, perceptual vision involves mapping early visual data into one or more concepts and then inferring meaning of the data based on prior experience and knowledge. Even in the case of IR images, the observer is looking at a picture of the scene displayed on some form of a monitor or display. The approaches of fuzzy and neuro-fuzzy systems will provide a robust alternative to complex semiempirical models for predicting observed responses to cluttered scenes. The

fuzzy-based approaches have been used to calculate the P_d of vehicles in different infrared scenes.

Probability of Detection (P_d) for Ground Targets

The development of the software that models the relationships among the various factors that affect the determination of the probability of detection is currently undergoing development. Some of these modeling factors are introduced in (57) to demonstrate the capability of the fuzzy and neuro-fuzzy approaches in predicting P_d with a 0.9 correlation to experimental values. The P_d value can be determined with the FLA using input parameters for the images shown in Fig. 4. The one output parameter is P_d. Figure 10 shows the FLA computed P_d's and the experimental P_d's for comparison. The correlation of the experimental P_d to the FLA-predicted P_d is 0.99. This result indicates the power of using the FLA to model highly complex data for which there would be many interrelated equations if one tried to model the detection problem as shown in Eqs. <xref target="W4110-mdis-0008 W4110-mdis-0009 W4110-mdis-0010 W4110-mdis-0011"/>.

APPLICATIONS OF INFRARED IMAGING SENSORS

Uncooled Pyroelectric IR Sensors for Collision Avoidance

Collision avoidance and vision enhancement systems are seen as an integral part of the next generation of active automotive safety devices (44, 45). Automotive manufacturers are evaluating the usefulness of a variety of imaging sensors in such systems (44). One potential application for automobiles is a driver's vision-enhancement system (53). This use of night-vision sensors as a safety feature would allow drivers to see objects at a distance of about 450 m, far beyond the range of headlights. Obstacles in the driver's peripheral visual field of view could be seen and recognized much sooner. Sensors that operate at wavelengths close to the electromagnetic frequency band of human vision (such as video cameras) provide images with varying degrees of resolution. However, the quality of the images (in terms of relative contrast and spatial resolution) acquired by such a camera degrades drastically under conditions of poor light, rain, fog, smoke, etc. One way to overcome such poor conditions is to choose an imaging sensor that operates at longer (than visual) wavelengths. The relative contrast in images acquired from such sensors does not degrade as drastically with poor visibility. However, this characteristic comes at a cost. The spatial resolution of the image provided by such sensors is less than that provided by an inexpensive video camera. Passive infrared sensors operate at a wavelength slightly longer than the visual spectrum. (The visual spectrum is between 0.4 and 0.7 μm, and the commonly used portions of the infrared spectrum are in the atmospheric "windows" that reside between 0.7 and 14 μm.) Hence the IR sensors perform better than video cameras (in terms of relative contrast) when visibility is poor. Also, because their wavelength of operation is only slightly longer, the quality of the image provided by an infrared sensor is comparable to that of a video camera (in terms of spatial resolution). As a result, infrared sensors have much potential for use in automotive collision avoidance systems (44, 46). Of all the different types of infrared detector technologies, this article considers two state-of-the-art infrared detectors that offer beneficial alternatives to an infrared sensor system for automotive and surveillance applications. The first alternative is based on a cooled FPA of CMOS PtSi infrared detectors that operate in the 3.4 to 5.5 μm wavelength band.

The second alternative is based on a staring, uncooled, barium strontium titanate (*BST*) FPA of ceramic sensors that operate in the 7.5 to 13.5 μm wavelength band. Under clear atmospheric conditions and at ranges less than 500 m, the 3.4 to 5.5 μm systems generate images with less contrast than the 7.5 to 13.5 μm systems. Dual-band field data show that the 3.4 to 5.5 band systems present more contrast between temperature extremes, whereas the 7.5 to 13.5 band systems show more detail in the overall picture. The TACOM Thermal Image Model (*TTIM*) is a computer model that simulates the appearance of a thermal scene seen through an IR imaging system (24). The TTIM simulates the sampling effects of the older single-detector scanning systems and more modern systems that use focal-plane, staring arrays. The TTIM also models image intensifiers. A typical TTIM simulation incorporates the image degrading effects of several possible atmospheric conditions by using low-resolution transmission (*LOWTRAN*), a computer model of the effects of atmospheric conditions on thermal radiation that was developed at the United States Air Force's Geophysics Laboratory. A particularly attractive feature of the TTIM is that it produces a simulated image for the viewer, not a set of numbers as some of the other simulations do. We refer the reader to Fig. 11 for a schematic representation of the TTIM. Examples of the usage of the TTIM are shown in Figs. 12,13, and 14. In Fig. 12, a CAD file of a tank is shown at the top, and the two lower images show the scene as seen through a TOW IR Imager at a certain range and then with rain added. Figure 13 shows how the TTIM compares different metrics used to quantify the visibility of a target. Figure 13 shows that simple metrics that assume a uniform target and background do not work. Figure 14 shows how the TTIM compares the performance of short and longwave IR imagers in the presence of rain. The TTIM has been used to simulate cooled and uncooled IR imaging systems and to compare their performance from the standpoint of automotive applications. Analogous comparisons exist in the current literature (47, 48).

The TTIM and NAC-VPM *together* allow comparing the performance of the two IR systems in terms of how good the quality of their images is for subsequent human perception/interpretation. Given that we have two images of the same scene, captured by using the two different infrared systems, we use the NAC-VPM to assess which of the two is *better*. The NAC-VPM is a computational model of the human visual system (49). Within the functional area of signature analysis, the unclassified model consists of two parts: early human vision modeling and signal detection. The early visual part of the model itself is made up of two basic parts. The first part is a color separation module, and the second part is a spatial frequency decomposition module. The color separation module is akin to

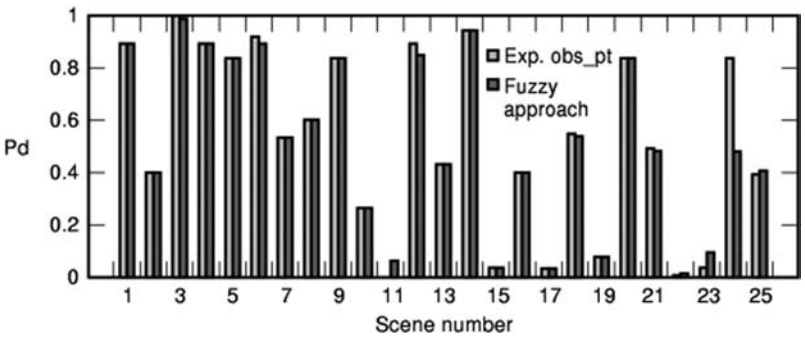

Figure 10. Graph of expected versus FLA predicted detection probabilities.

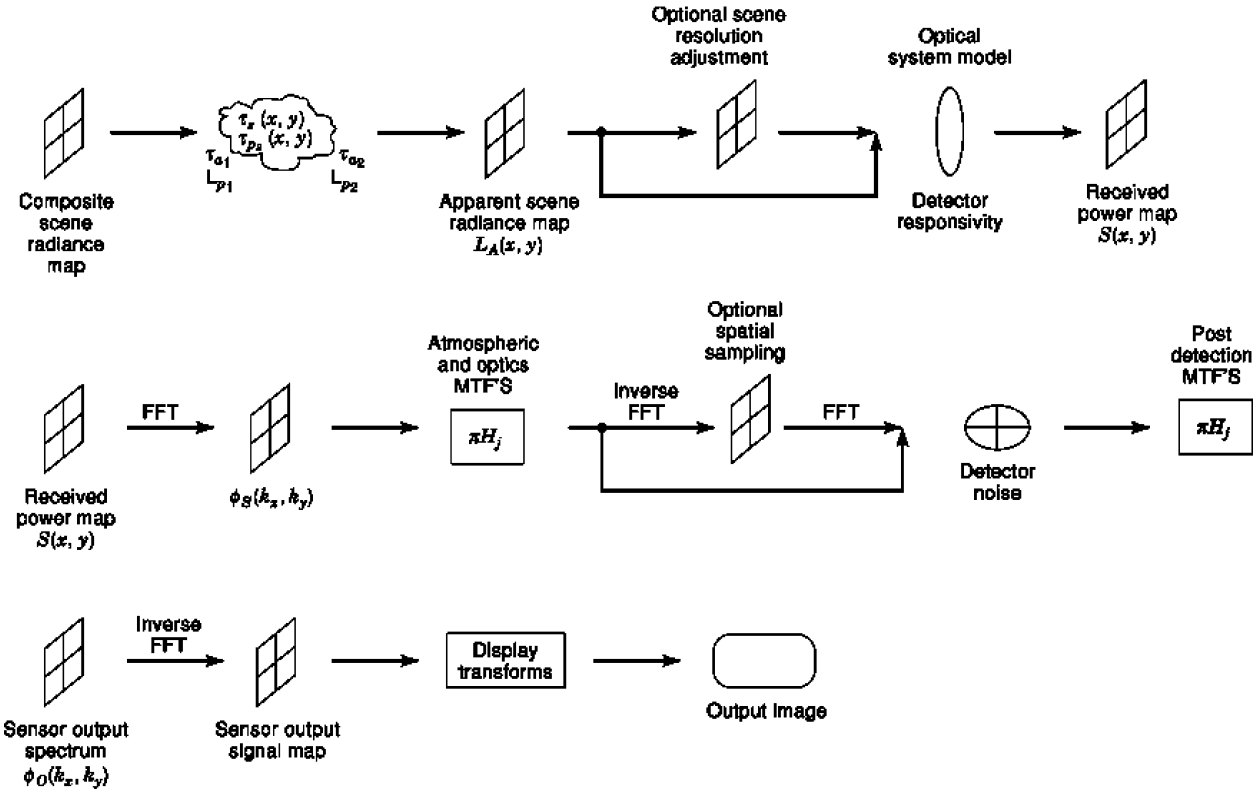

Figure 11. Schematic of the TTIM computer model.

the human visual system. The spatial frequency decomposition system is based on a Gaussian–Laplacian pyramid framework. Such pyramids are special cases of wavelet pyramids, and they represent a reasonable model of spatio-frequency channels in early human vision (50). See Fig. 15 for a schematic representation of NAC-VPM. Figure 16 shows how the TTIM and NAC-VPM together are used to determine which spatial frequencies and features of a vehicle are the most visible.

Simulation of Infrared Sensors

This section presents the simulation of cooled and uncooled infrared imaging systems using the TTIM. Specifically, the input to the TTIM was the actual thermal images of commercial vehicles in a typical road scene, which were resampled using the TTIM. The initial infrared images were taken at TARDEC with the pyroelectric sensor from Raytheon. Examples of the way rain affects the quality of the sensor displayed image are presented. *Target* is synonymous with the *object of interest* in the scene and *no target* means the image with the *object of interest removed.* This type of simulation is a substantial first step to providing a means for comprehensively evaluating and comparing sensor systems. The ability to simulate the sensors provides a means for exactly repeating imaging experiments and measurements, difficult to achieve in field trials. Also, the ability to simulate the sensors provides the ability to exercise control over the imaging conditions. In the cooled infrared systems, for example, it is important to provide proper temperature shielding during field trials. Otherwise, the quality of the images acquired from the infrared system is badly affected, and it negatively affects the validity of subsequent comparisons between sensor systems. By simulating cooled infrared systems, such difficulties can be avoided. Figure 17 shows simulated infrared images of typical commercial vehicles when the viewing distance (the

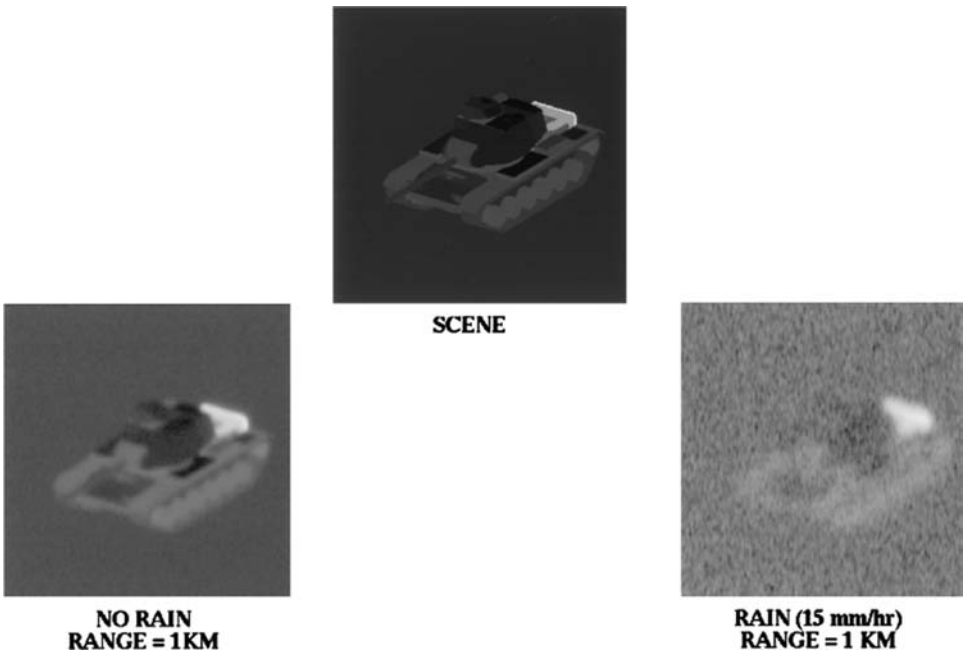

Figure 12. CAD image of tank and simulated range and rain degradation using TTIM.

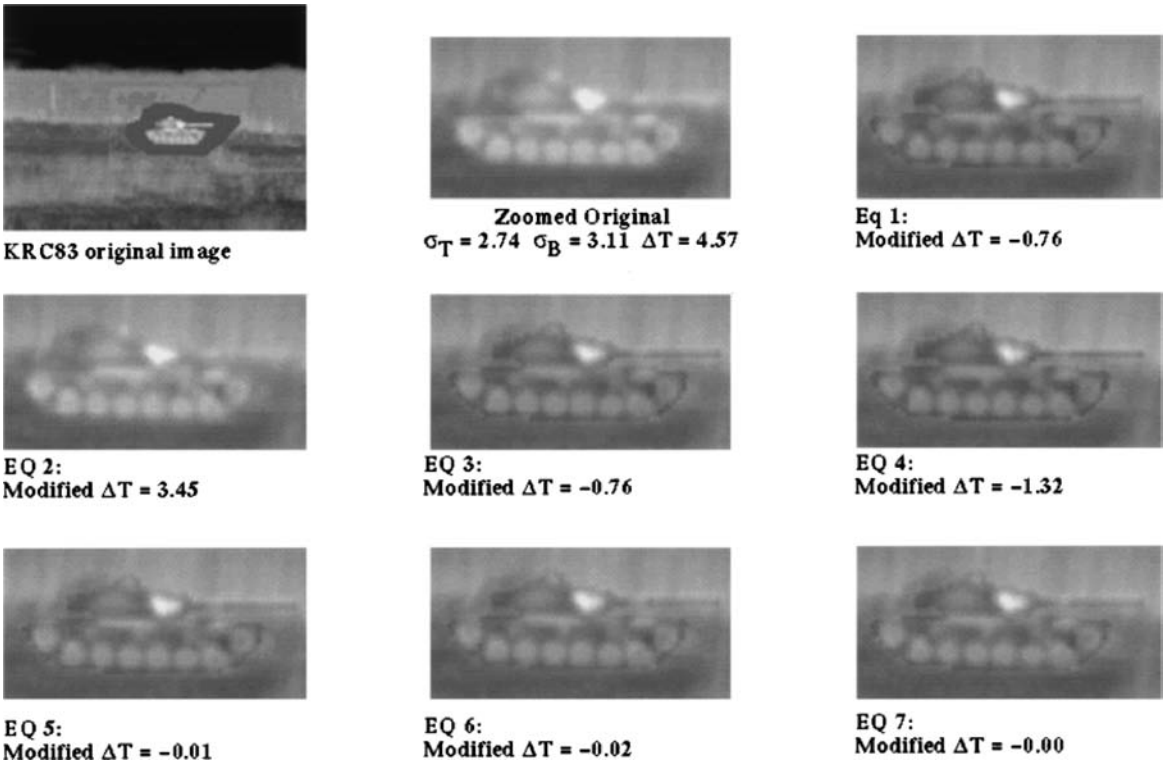

Figure 13. Comparison of thermal target metrics using TTIM.

distance between the vehicle and the sensor) is fixed and the amount of rainfall under which the image is acquired increases. This is done for both the cooled and uncooled cases by inputting into the TTIM the thermal image containing the target and no-target image. The images have been resampled according to the specific sensor and then degraded by rain and fog. The uncooled images are in the left column and the cooled images are in the right column. The top row is the clear case with and without the object of interest, which is the car at the center of the picture. The range for all the pictures is 70 m. The second row is for the case of fog. As one goes down the columns of images, the rain rate is 1, 12.5, 25, 37.5, and 50 mm/h, respectively. The images show that the longwave, uncooled camera provides

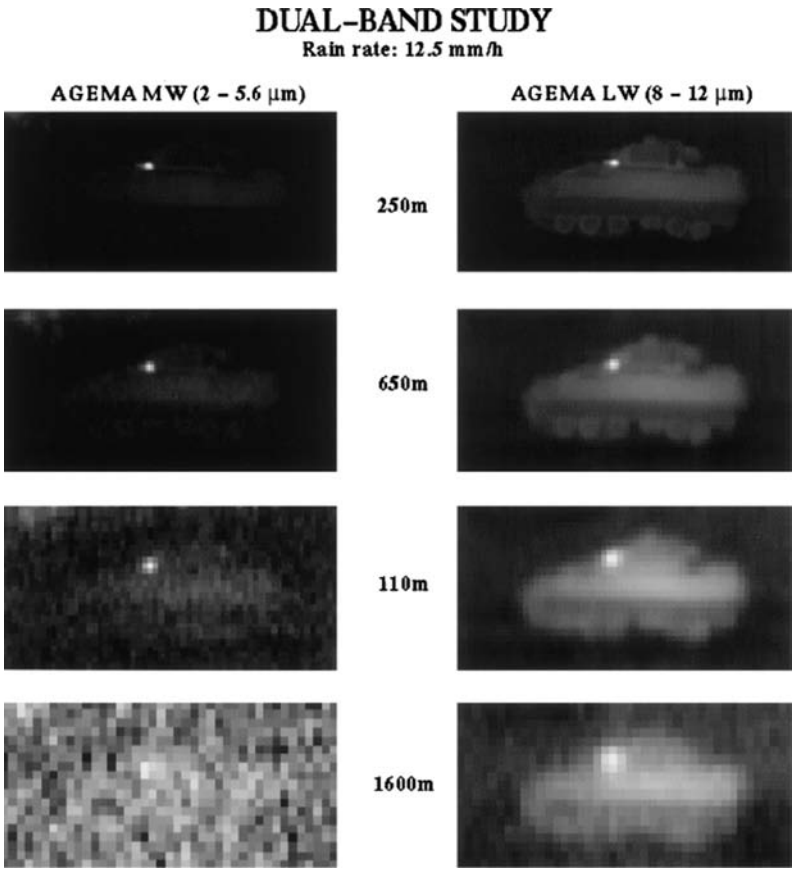

Figure 14. Dual-band study using TTIM.

a higher contrast picture under all conditions. The system (courtesy of Mr. Sam McKenney of Raytheon) used by the authors to take the original data is shown in Fig. 18. Figure 19 shows simulated images from the uncooled sensor that were resampled to represent ranges at 30 to 90 m.

Sensor Image Comparison

The NAC-VPM was used to compare the quality of images acquired from the cooled and the uncooled, infrared imaging systems through rain and fog. With the NAC-VPM one may obtain the SNR and a psychophysical measure of detectability d' (58) in each of the images for a vehicle of interest. The input to the TVM was the target and no-target images, corresponding to the infrared systems (54). In Fig. 20 the highest SNR of all frequency channels is plotted as a function of the rain rate. The curve in Fig. 20 with the higher whole image SNR is that of the uncooled pyroelectric FPA. The image with the higher SNR has a greater contrast and is easier to interpret. The object of interest in a scene with the higher d' has a higher conspicuity and is therefore easier to see. Figure 21 shows the predicted visibility of the vehicles when viewed through the sensors and atmosphere. The two curves in Fig. 21 are the detectabilities of the target vehicle predicted by the visual model. For this particular case, the conspicuity of the target seen through the uncooled 7.5 to 13.5 band has the higher predicted conspicuity. Using the TTIM, one may successfully simulate both infrared imaging systems. The 7.5 to 13.5 band has more background radiance in the scenes which tends to add more gray to the image as the rain-rate increases, whereas, the 3.4 to 5.5 band gets grayer with increasing rain rate primarily because of radiance loss due to scattering. These model predictions are consistent with infrared field images of test patterns through both bands in the rain. Scattering losses are compounded by the shape of the Planck blackbody distribution. The shape of the blackbody curves at a temperature of 300 K show that the 7.5 to 13.5 band has almost a factor of 2 more energy. By using the NAC-VPM, the two sensors were compared. In each of the spatial frequency channels found in early vision among humans, a measure of detectability for an object and background of interest is found. The SNR versus rain rate for both the sensors can be plotted, and the variation in the SNR, as the amount of rainfall under which the images are acquired increases, is obtained. Simulations show that (1) because the 7.5 to 13.5 band has more excitance than the 3.4 to 5.5 band and (2) the transmittance is nearly a factor of 1.5 better in rain than the 7.5 to 13.5 band, (3) coupled with the fact that the uncooled imagery was excellent in quality, the 7.5 to 13.5 band, uncooled pyroelectric sensor is the better multipurpose sensor. In addition, the unit used for data collection was in fact several years old, and there has since been a 50% increase in detector sensitivity along with improvements in the detector uniformity and system implementation. Sensor comparisons are one aspect of collision avoidance and vision enhancement. There are a number of other human factors and social issues associated with the *science of collision avoidance,* as pointed out in (45).

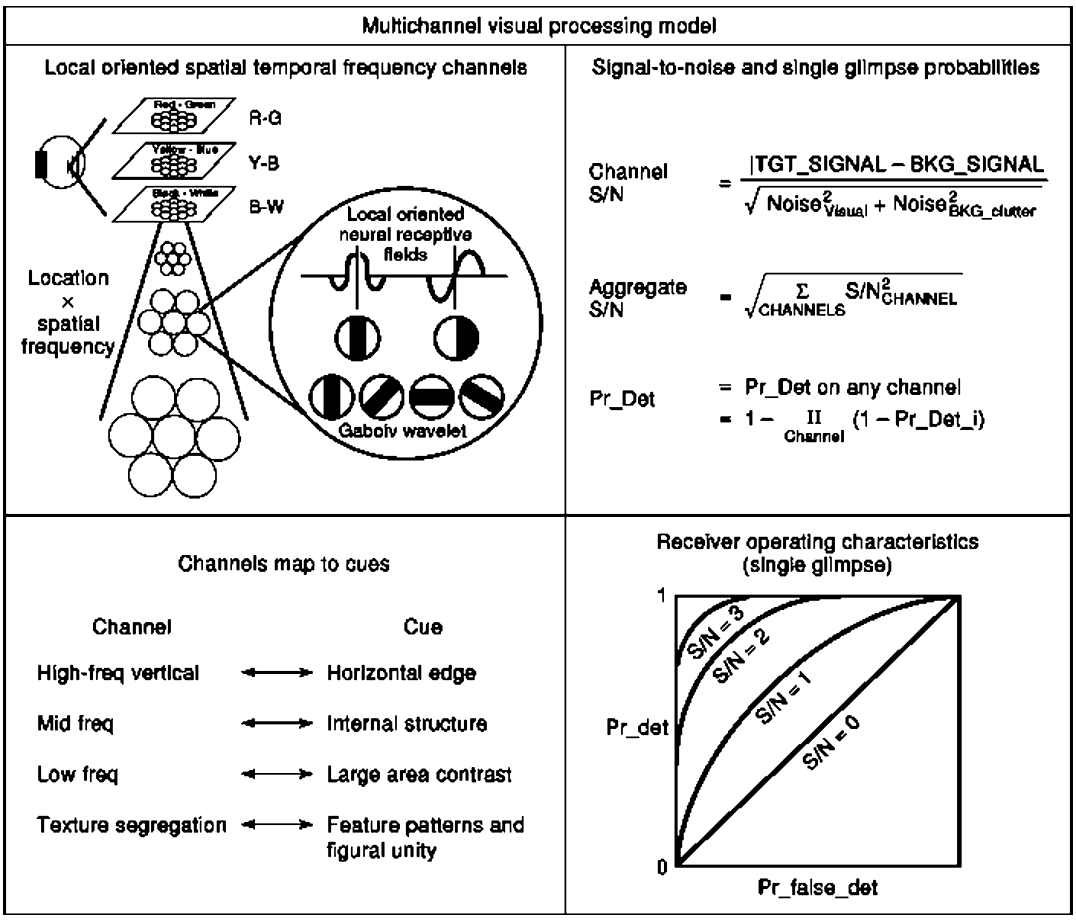

Figure 15. Schematic of NAC-VPM computer model.

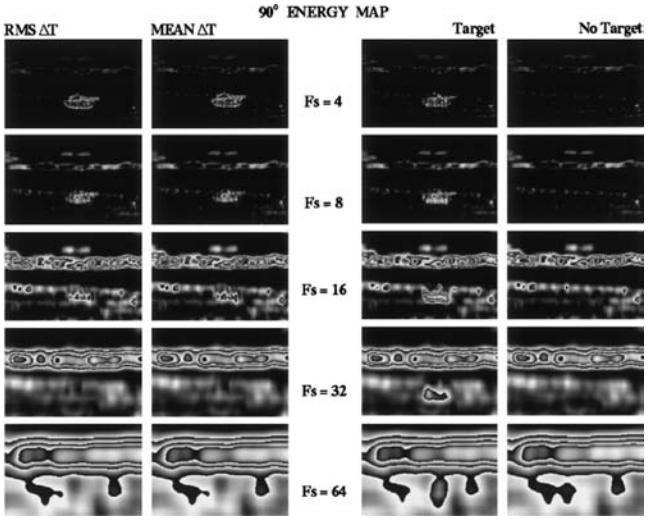

Figure 16. Use of TTIM and NAC-VPM to determine spatial frequencies of greatest visibility of a baseline vehicle.

TARDEC Visual and Infrared Perception Laboratory (*VPL*)

The TARDEC National Automotive Center (*NAC*) is developing a dual-need visual and infrared perception laboratory as part of a Cooperative Research and Development Agreement (*CRDA*) between Army Materiel Command (*AMC*) and local auto companies. Dual use has become an important term which means that the technology developed by the US Army could be used by the civilian sector, and vice versa. There are many applications of IR imagers; in particular, they are used for defense and civilian collision avoidance applications. As part of the performance assessment of the imagers, a perception laboratory can be used to determine the performance of various sensors in terms of enhancing the scene in the field-of-view of an observer. TARDEC researchers are using this facility

Figure 17. Cooled and uncooled sensor images at fixed range.

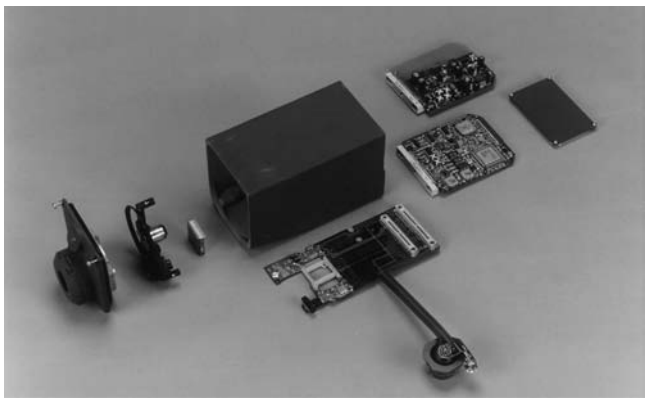

Figure 18. Texas Instrument uncooled thermal imager.

to calibrate and validate human performance models for evaluating visual collision avoidance countermeasures for commercial and military vehicles on the nation's highways. The laboratory is also being used to collect baseline data on the human visual perception of various types of ground vehicles and treatments to those vehicles.

Figure 22 shows a schematic of the fully automated data acquisition and analysis hardware used in the laboratory. A unique capability of the laboratory is the magnetic head tracker attached to the observer which relays signals to the control computer for the correct image display at an appropriate time during the intersection search scenario. Additional recently upgraded capabilities include a combination headtracker and eyetracker to record instantaneous foveal fixation relative to the scene. The existing laboratory configuration could also be used to present infrared images to observers. The laboratory experiments have several advantages over field-test exercises including better control over observer stimuli, larger sample sizes, and lower cost. In particular, laboratory perception tests offer a viable and economic way of *augmenting* and *complementing* field test data by using image simulation techniques to extend the

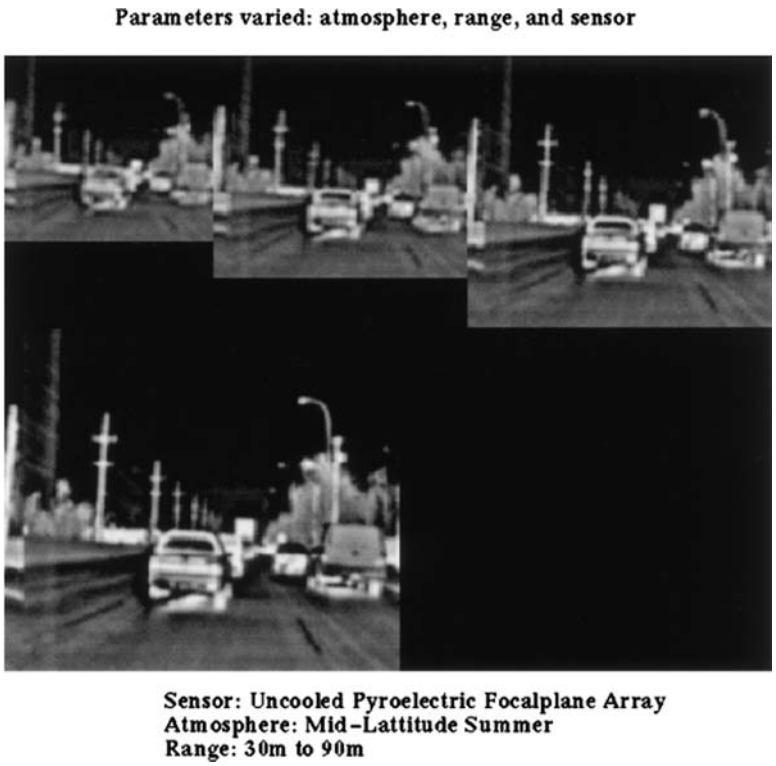

Figure 19. Uncooled imager simulation at four ranges.

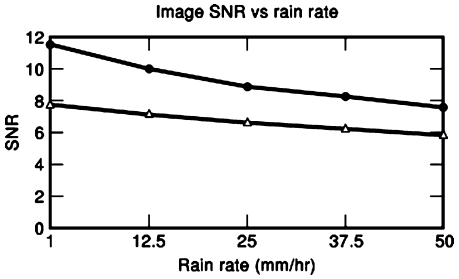

Figure 20. Image SNR versus rain rate.

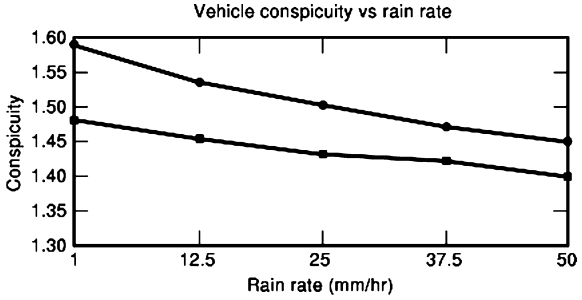

Figure 21. Conspicuity versus rain rate.

range of conditions and target/background signatures beyond the original field test conditions. These techniques are particularly useful for virtual prototyping of military and civilian applications. An example of dual-need functionality of the VPL is that the recent calibration of the NAC-VPM in the laboratory for automotive use also worked well for camouflaged vehicles.

Visual Perception Laboratory Facilities

Figure 23 shows a view of the main test area viewed through the control room window in the laboratory. The entire facility consists of a 2500 ft^2 area which can accommodate vehicles ranging in size up to the Bradley IFV. This scene also shows that a half-car mock-up used in a perception experiment surounded by the three video projection screens which display the driver's front, left, and

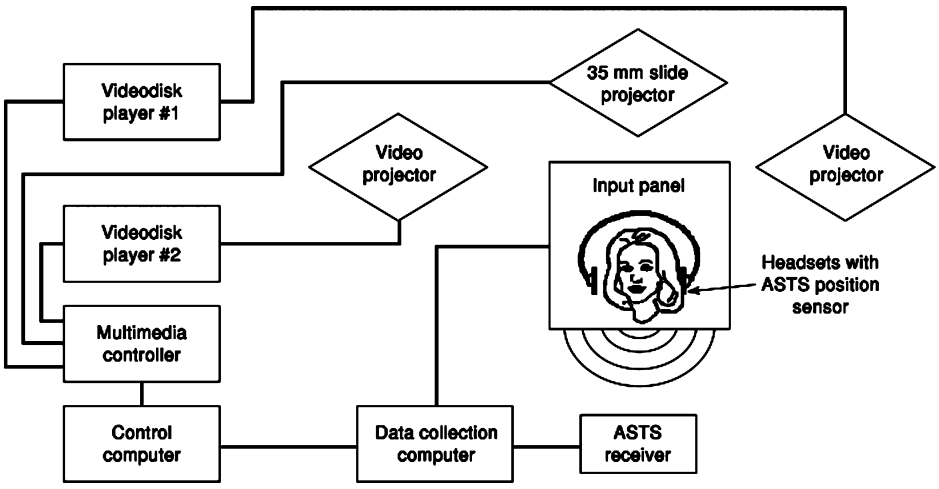

Figure 22. Current equipment setup for the visual perception laboratory.

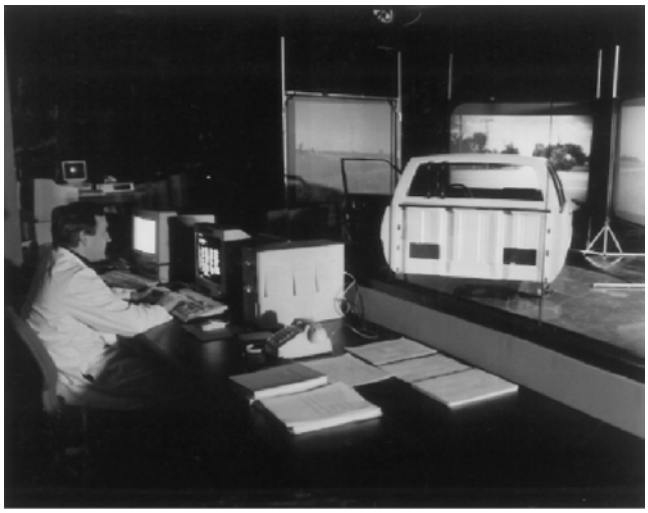

Figure 23. TARDEC VPL.

Figure 24. Visual scene in TARDEC VPL as seen by driver.

right views of the intersection traffic. Figure 24 shows a visual scene containing camouflaged targets located along a tree line depicted from behind the driver's head position through the front windshield of a HMMWV. Visual perception experiments conducted with such scenes will allow Army researchers to study a wide field-of-regard (*FOR*) search-and-target-acquisition (*STA*) strategies for military vehicles.

Further upgrades to the VPL scheduled to occur during the next year will be the addition of three screens and LCD projectors to provide a five-screen wraparound effect and wide field-of-regard as required for search and target

acquisition performance assessment of ground vehicle systems.

Infrared Imaging for Ice Detection and Situational Awareness

Following are two examples of the use of different parts of the infrared spectrum, near and far, for remote nondestructive testing and increased situational awareness. The first example describes an infrared system for remote detection of ice and the second example describes an infrared and visible fused system for situational awareness.

As part of a Space Act Agreement between NASA-Kennedy Space Center (*KSC*) and the U.S. Army Tank Automotive Research Development and Engineering Center (*TARDEC*), members of TARDEC's Visual Perception Lab (*VPL*) performed a technology search and laboratory evaluation of potential electro-optical systems capable of detecting the presence and determining the thickness of ice on Space Transportation System (*STS*) External Tank (*ET*) Spray-On-Foam Insulation (*SOFI*), see Figure 25. The SAA and subsequent evaluation activity resulted from discussions between NASA-KSC and the Army following the Columbia Shuttle accident. NASA sought a fresh approach to seemingly intractable ice accumulation and assessment problems that had plagued them since the earliest days of the STS Program. The VPL team, having expertise in imaging sensors, desired to contribute in some way to NASA's Return to Flight planning and accomplishment.

Previous research by VPL investigators, following earlier NASA inquiries, indicated that it might be possible to detect and image ice-covered areas with an infrared (*IR*) camera. In addition it was realized that methods were needed to detect clear ice (transparent to the naked eye), and to discriminate between ice, frost, and water on ET SOFI surfaces. A technology search followed by members of the VPL resulted in a selection of two electrooptical systems using infrared as candidates for further investigation. The VPL comparison of these systems, testing, and analyses was the subject of the first report submitted to NASA-KSC in June 2004. As a result of that report, VPL investigators and NASA engineers determined that a system developed by MacDonald, Dettwiler and Associates Ltd. (MDA–formally known as MDR) of Canada offered the greatest potential to support T-3 hour ice debris team detection and evaluation activities on the launch pad prior to STS launches.

NASA's initial desire was that the system be capable of detecting ice with a thickness and the diameter of a U. S. quarter (approximately, 1/16 inch thick [0.0625 inch] and one inch in diameter)–in essence the Launch Commit Criteria (*LCC*) for safe vehicle ascent. In addition, the system was to be passive (without emissions), portable for use by the NASA ice debris detection team on access platforms at T-3 hours, and able to meet launch complex safety requirements (i.e. be explosion proof and within EMI/EMC limits).

Description of the MDA System

The MDA system uses a low power near-infrared Xenon strobe to illuminate a surface on which there may be ice–in this case, ET SOFI. After illumination of the SOFI surface, electromagnetic energy is reflected back and focused on to an IR (1.1 to 1.4 micron, [Gregoris, 60]) sensor. An un-cooled focal plane array sensor provides inputs to a linked computer. Based on the electromagnetic theory of reflection of light at the surface of a dielectric (ice in this case), the computer estimates the thickness of ice, if present. Various ice thickness ranges are color-coded (e.g., blue = 0.020–0.029 inch, green = 0.030–0.039 inch, yellow = 0.040–0.049 inch, red $\geq$0.050 inch) [59] on the system monitor to help the operator interpret values quantitatively. A circular "bulls-eye" is shown on the system display to align a small -target area. The average measured ice thickness from pixels located in the bulls-eye (64 pixels 8×8), is displayed on-screen in a field labeled "tkns in" (i.e. thickness inches). The system and its components (sensor, VHS recorder, and battery power supply) are contained in N_2 purged enclosures, and are mounted on a two wheeled cart provided by NASA as shown in Figure 26 below.

Referring to Figure 27 below, as light is incident on a thin dielectric (e.g. ice), a fraction of the light is reflected at the air/dielectric interface, and the rest of the light is transmitted through the dielectric. The transmitted fraction propagates through the dielectric until it reflects off the substrate. The light reflected off the substrate returns through the dielectric until it reaches the dielectric/air interface, where it is again partially reflected into the dielectric and the air. Some absorption of the light occurs as it travels through the dielectric. The internal reflection continues until all the light is absorbed completely by the dielectric.

For a dielectric of thickness d, the effective reflectance, R_e (λ, θ), of the dielectric layer is given by Equation 12 below,

$$R_e(\lambda, \theta_i) = R(\lambda, \theta_i) + [\frac{R_w(\lambda)(1 - R(\lambda, \theta_i))^2 e^{-2a(\lambda)d}}{1 - (R_w(\lambda)R(\lambda, \theta_i))^2 e^{-2a(\lambda)d}}], \quad (12)$$

where,

R_e *(*λ*,* θ_i*)* is the effective reflectance
R*(*λ*,* θ*)* is the dielectric spectral reflectance
a *(*λ*)* is the spectral absorptivity
R_w *(*λ*)* is the substrate spectral reflectance.

Using specific sub-bands within the near IR region of 1.1–1.4 microns, the spectral contrast is defined by,

$$C = [\frac{R_l - R_u}{R_l + R_u}], \quad (13)$$

where l, and u are the lower and upper bands respectively in Equation 13. Measurement of the reflected energy and the computation of the spectral contrast allows for the detection of ice on a surface and the estimation of the thickness d, of the ice on that surface. Below in Figure 28, (chart from U.S. Patent # 5,500,530 [60]), the reflectance is plotted versus wavelength for 0.5 mm ice and water layers with light incident normal to the surface. It is clear from Figure 28 that the IR reflectance of water and ice is very different and linear over a long range.

During the year 2006, VPL and NASA ice debris team members tested the MDA ice camera in a hanger at the

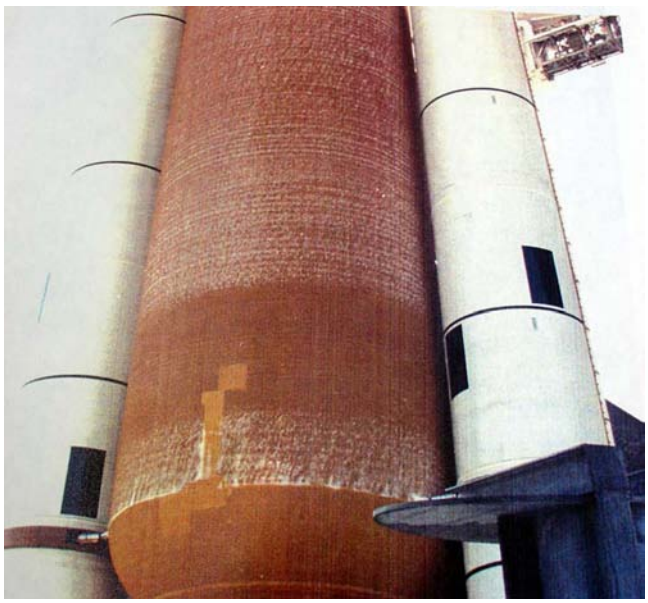

Figure 25. Frost and ice on the space shuttle ET SOFI (Courtesy of NASA KSC).

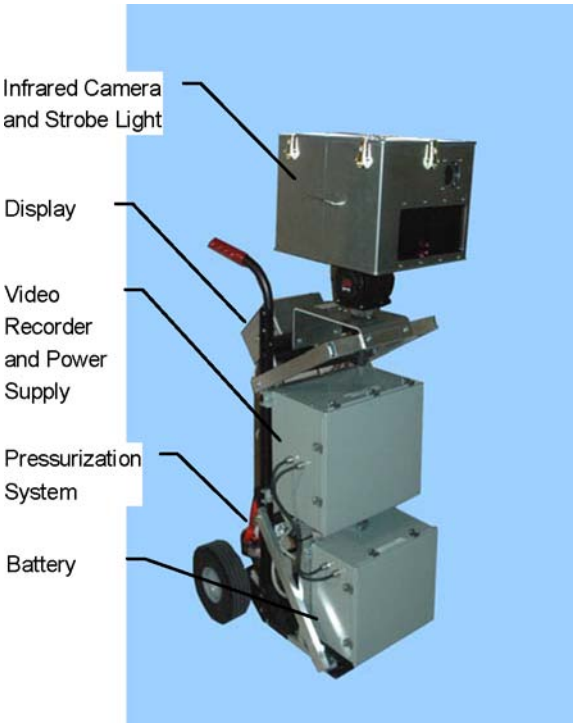

Figure 26. MDA ET Inspection System Cart (courtesy of MDA Corp.).

Selfridge Air National Guard Base (*SANG*) in southeastern Michigan. A sample image of the display of the camera is shown below in Figure 29. Future tests and system modifications are being planned at the time of this article.

The images below in Figure 30 are an example of the use of image fusion to show surface and subsurface defects in a thermal protective tile used on the shuttle orbiter. The top image is the IR image, the second image is the visible image, and the bottom most image is the fused image of the IR and visible. The type of fusion performed was contrast, Laplacian pyramid, and the imaging was done using cameras in the TARDEC Visual Perception Lab.

INFRARED IMAGING AND IMAGE FUSION USED FOR SITUATIONAL AWARENESS

A requirement for armored vehicles of the future is to have a system that is able to provide close-in situational awareness and understanding to the crew within the whole 360 degree hemisphere (Figure 31) of the vehicle. TACOM, Ford and Sarnoff Laboratories are partnering to develop, test and evaluate prototype systems to provide situational awareness.

Elmo QN42 visual cameras (Figure 32) are used in the present system because of their small size and excellent

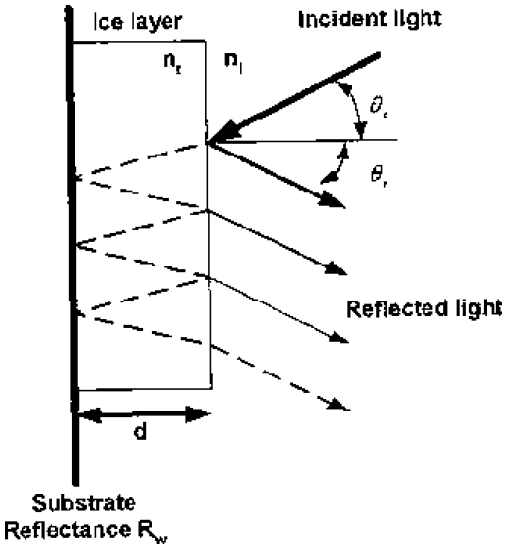

Figure 27. Reflection of light from a thin ice layer.

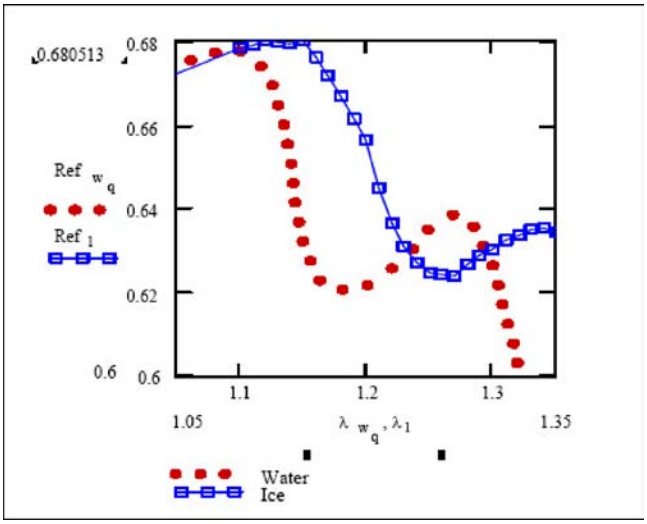

Figure 28. Computed spectral reflectance of ice and water versus wavelength [60].

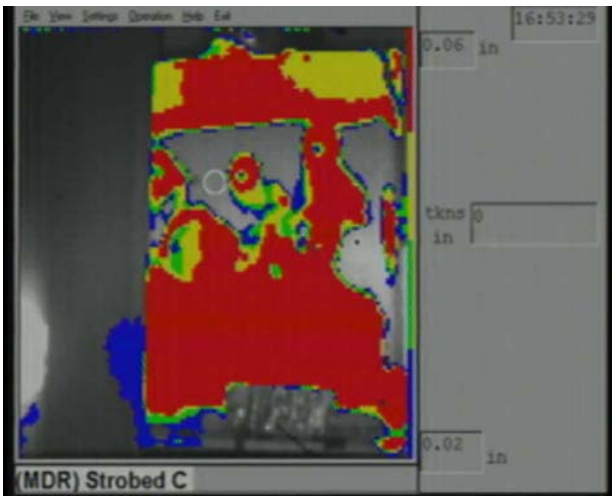

Figure 29. MDA Ice camera display of ice covered SOFI panel (picture from SANG tests) Red areas indicate ice thickness of 0.0625 in.

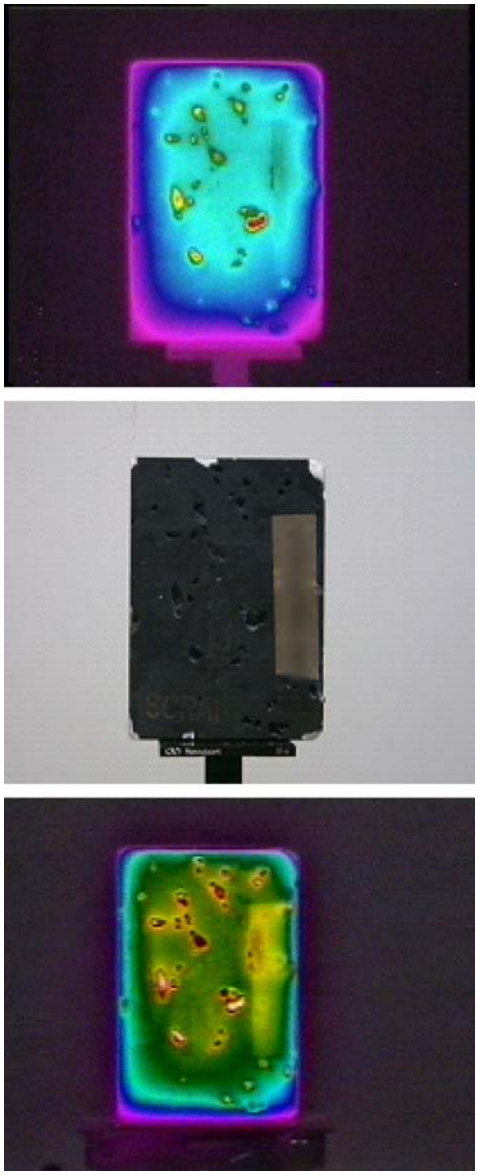

Figure 30. IR, visible and fused image of thermal protective tile.

Figure 31. 360 degree panoramic fusion concept picture.

Figure 32. Elmo QN42 Camera used in TARDEC system.

color fidelity. The cameras have a field of view of approximately 53 degrees by 39 degrees. The Elmo cameras have a 410,000 pixel color CCD that results in 786 (V) X 470 lines (H) resolution with simultaneous Y/C and composite video outputs.

Indigo Omega infrared cameras (Figure 33) were also selected because of their small size and clear image and have an image array resolution of 160 by 120 pixels, with a 51 by 51 micron pixel size. The detector is an uncooled micro bolometer. The infrared cameras are fitted with 8.5 mm lenses that provide a field of view of approximately 55 by 40 degrees. The Indigo Omega cameras are sensitive to the 7.5 to 13.5 micron band of the electromagnetic spectrum.

There are four visible cameras and four IR cameras in each of the housings in the front and rear of the vehicle, hence a total of eight visible and infrared cameras. The output of the eight cameras are combined using multiplexers and with the Sarnoff stitching and image registration software provide a panoramic view that is scrollable and adjustable in magnification. The imagery from the cameras is combined, registered, and fused to provide a real-time panoramic stitched view of the world around the vehicle onto which they are mounted. Figure 34 shows the sensor systems attached to the Lincoln Navigator. The sensors are in the open configuration for testing and characterization. Future plans for hardening include the use of transparent covers and lenses and a smaller housing.

A Lincoln Navigator was used as a test vehicle prototype for of several reasons: 1) such a test platform for the cameras is practical for driving around and testing the camera system in the metropolitan areas, and 2) the Navigator platform has ample space in the back and permits a convenient platform to demonstrate the system.

APPENDIX A

Abbreviations

ET:	External Tank
FOV:	Field of View
FSS:	Fixed Service Structure
IR:	Infrared
LCC:	Launch Commit Criteria
LH2:	Liquid Hydrogen
LN2:	Liquid Nitrogen
LO2:	Liquid Oxygen
MDA:	MacDonald, Dettwiler and Associates Ltd.
SAA:	Space Act Agreement between NASA and TARDEC
SOFI:	Spray-on Foam Insulation
SOW:	Statement of Work
STS:	Space Transportation System
SWIR:	Shortwave infrared
TARDEC:	Tank Automotive Research, Development,and Engineering Center
VPL:	Visual Perception Laboratory at TARDEC

SUMMARY

Infrared imaging is playing an increasingly important role in several application areas in the US Army and in the automobile companies for collision avoidance, nondestructive evaluation of materials, medical diagnostic imaging, and astronomy.

Figure 33. Indigo Omega IR camera used in TARDEC system.

Figure 34. Front and rear camera assemblies mounted on a TARDEC Lincoln Navigator with prototype 360 degree image fusion system.

BIBLIOGRAPHY

1. J. E. Palmer J. D'Agostino T. J. Lillie *Infrared Recognition and Target Handbook*, NVEOL, Ft. Belvoir, VA, 1982.
2. *Britannica World Language Edition of Funk and Wagnalls Standard Dictionary*, Encyclopedia Britannica, vol. 1, Chicago, 1961, p. 650.
3. M. Schlessinger *Infrared Technology Fundamentals*, 2nd ed., New York: Marcel Dekker, 1995, p. 200.
4. L. F. Pau M. Y. El-Nahas *An Introduction to Infrared Image Acquisition and Classification Systems*, Research Studies Press, 1983.
5. J. L. Miller *Principles of Infrared Technology*, New York: Van Nostrand Reinhold, 1994.
6. M. Schlessinger *Infrared Technology Fundamentals*, 2nd. ed., New York: Marcel Dekker, 1995.
7. R. W. Mangold *Infrared Theory, Temperature Developments*, Stamford, CT: Omega Engineering, Inc.
8. P. Klocek, ed. *Handbook of Infrared Optical Materials*, New York: Marcel Dekker, 1991.
9. E. L. Dereniak G. D. Boreman *Infrared Detectors and Systems*, New York: Wiley, 1996.
10. *Table on Infrared System Characteristics*, courtesy of Mr. Luke Scott, NVESD, 1992.
11. C. Contini R. Honzic Staring FPA Modeling Capability, *SPIE*, **636**: 60, 1986.
12. B. L. O'Kane C. P. Walters J. D'Agostino *Report on Perception Experiments in Support of Thermal Performance Models.* NVL Report, 1993.
13. B. L. O'Kane *et al. Target signature metrics analysis for performance modeling*, 1993.
14. D. Schmieder M. Weathersby Detection performance in clutter with variable resolution, *IEEE Trans. Aerosp. Electron. Syst.*, **AES-19**: 1983.
15. W. Reynolds Toward quantifying infrared clutter, in *Characterization, Propagation, and Simulation of Infrared Scenes*, SPIE vol. 1311.
16. M. R. Weathersby D. E. Schmieder An experiment for quantifying the effect of clutter on target detection, in *Infrared Technology*, SPIE vol. 510, 1984, pp. 26–33.
17. W. Reynolds A. L. LaHaie R. K. Baratono *Standard Scenes Program for Establishing a Natural Scenes Data Base*, KRC, DAAE07-85-G-R007, 1989, p. 49.
18. B. L. O'Kane *et al. Target signature metrics analysis for performance modeling*, March 1993.
19. S. R. Rotman E. S. Gordon M. L. Kowalczyk Modeling human search and target acquisition performance: III. Target detection in the presence of obscurants, *Opt. Eng.*, **30** (6): 1991.
20. D. Marr *Vision—A Computational Investigation into the Human Representation and Processing of Visual Information*, New York: W. H. Freeman, 1982.
21. P. Burt E. Adelson The Laplacian Pyramid as a Compact Image Code, *IEEE Trans. Commun.*, **COM-31**: 532–540, 1983.
22. S. R. Rotman E. S. Gordon M. L. Kowalczyk Modeling human search and target acquisition performance: III. Target detection in the presence of obscurants, *Opt. Eng.*, **30** (6): 1991.
23. T. J. Doll D. E. Schmeider Observer false alarm rate effects on target resolution criteria, *KRC Symp. Proc.*, 1992, pp. 206–218.
24. J. M. Hall E. T. Buxton T. J. Rogne *Tacom Thermal Image Model Ver. 3.1, Technical Reference and User Guide*, Dec. 1989.
25. T. Cook *et al.* The impact of aliasing on vehicle detectability, *Proc. 3rd Annu. Ground Target Modeling Validation Conf.*, August 1992.

26. T. Meitzler G. Gerhart P. Collins A comparison of 3–5 and 8–12 micron sensors, *Proc. Infrared Imaging Syst.: Des., Anal., Modeling, Testing IV SPIE Conf.*, April 1994.
27. W. K. Pratt *Digital Image Processing*, New York: Wiley, 1978, p. 508.
28. T. Meitzler W. Jackson D. Bednarz A semi-empirical study of background clutter and texture in infrared scenes, *Proc. 3rd Annu. Ground Target Modeling Validation Conf.*, August, 1992.
29. S. R. Rotman, *et al.* Modeling human search and target acquisition performance: V. Search strategy, *Opt. Eng.*, April 1996, submitted.
30. T. J. Meitzler *Modern Approaches to the Computation of the Probability of Target Detection in Cluttered Environments*, Ph.D. Thesis, Wayne State University, 1995.
31. M. O. Freeman Wavelets-signal representations with important advantages, *Opt. Photonics News*, **4** (8): 8–14, 1993.
32. H. H. Szu, ed. *Wavelet Applications*, SPIE Proc. 2242, SPIE, Bellingham, WA, 1994.
33. T. Meitzler *et al.* Wavelet transforms of cluttered images and their application to computing the probability of detection, *Opt. Eng.*, **35** (10): 3019–3025, 1996.
34. G. Gerhart *et al.* Target Acquisition Methodology for Visual and Infrared Imaging Sensors, *Opt. Eng.*, **35** (10): 3026–3036, 1996.
35. S. Mallet S. Zhong Characterization of signals from multiscale edges, *IEEE Trans. Pattern Anal. Mach. Intell.*, **14**: 710–732, 1992.
36. L. Zadeh Fuzzy Sets, *Information and Control*, **8**: 338–353, 1965.
37. E. Mamdani S. Assilian Applications of fuzzy algorithms for control of simple dynamic plant, *Proc. Inst. Elec. Eng.*, **121**: 1585–1588, 1974.
38. T. Munakata Y. Jani Fuzzy systems: An overview, *Commun., ACM*, **37** (3): 69–76, 1994.
39. R. Mizoguchi H. Motoda (eds.) AI in Japan: Expert systems research in Japan, *IEEE Expert*, **10** (4): 14–23, 1995.
40. E. Cox *The Fuzzy Systems Handbook: A Practitioner's Guide to Building, Using, and Maintaining Fuzzy Systems*, Cambridge, MA: AP Professional, 1994.
41. D. G. Schwartz *et al.* Applications of fuzzy sets and approximate reasoning, *IEEE Proc.*, **82** (4): 482–498, 1994.
42. T. Terano K. Asai M. Sugeno *Fuzzy Systems and Its Applications*, Cambridge, MA: AP Professional, 1992.
43. M. Gupta G. Knopf Fuzzy logic in vision perception. *Robots Comput. Vision XI*, SPIE 1992, vol. 1826, pp. 300–316.
44. R. K. Jurgen The electronic motorist, *IEEE Spectrum* **32** (3): 37–48, 1995.
45. R. K. Deering D. C. Viano Critical success factors for crash avoidance countermeasure implementation, *Proc. Int. Congr. Transp. Electron.*, 1994, pp. 209–214.
46. S. Klapper B. Stearns C. Wilson Low cost infrared technologies make night vision affordable for law enforcement agencies and consumers, *Proc. Int. Congr. Transp. Electron.*, 1994, pp. 341–345.
47. G. A. Findlay D. R. Cutten Comparison of performance of 3–5 and 8–12 micron infrared system, *Appl. Opt.*, **28**: 5029–5037, 1989.
48. T. W. Tuer *Thermal imaging systems relative performance: 3–5 vs 8–12 microns*, Tech. Rep., AFL-TR-76-217.
49. G. H. Lindquist G. Witus *et al.* Target discrimination using computational vision human perception models, *Proc. SPIE Conf. Infrared Imaging Syst.: Des. Anal., Modeling Testing*, 1994, vol. 2224, pp. 30–40.
50. J. Malik P. Perona Preattentive texture discrimination with early vision mechanisms, *J. Opt. Soc. Am.*, **7**: 923–932, 1990.
51. A. B. Watson Detection and recognition of simple spatial forms, NASA Tech Memo No. 84353, Natl. Aeronautics Space Administration, Moffett Field, CA, 1983.
52. P. W. Kruse Thermal imagers move from the military to the marketplace, *Photonics Spectra*, 103–108, 1995.
53. Lakshmanan *et al.* Simulation and comparison of infrared sensors for automotive collision avoidance, *1995 SAE Int. Congr. Exposition*, Feb. 1995.
54. R. E. Flannery J. E. Miller Status of Uncooled Infrared Imagers, 1689, in *Infrared Imaging Systems*, 1992, SPIE vol. 1689, pp. 379–395.
55. D. E. Burgess Pyrolectrics in a harsh environment, in *Infrared Detectors and Arrays*, 1988, SPIE vol. 930, pp. 139–150.
56. T. Meitzler *et al.* Fuzzy logic approach to computing the probability of target detection in cluttered environments, *Opt. Eng.*, **35** (12): 1996.
57. W. Wolfe G. Zissis (eds.) *The Infrared Handbook*, revised ed., Environmental Res. Inst. Michigan, 1989, pp. 8–19.
58. G. Gescheider *Psychophysics Method, Theory, and Application*, Lawrence Erlbaum, 1985.
59. MD Robotics Prototype Ice Detection Camera User Manual, Rev. 3.0, 6 January 2005, pg. 18.
60. United States Patent # 5,500,530, March 1996, inventor: Gregoris; Dennis J., assignee: SPAR Aerospace Limited (Brampton, Ontario, Canada).

THOMAS J. MEITZLER
GRANT R. GERHART
EUIJUNG SOHN
HARPREET SINGH
KYUNG–JAE HA
US Army Tank-Automotive and Armaments Command, Warren, MI
Wayne State University, Detroit, MI